

# Supersolid-like solitons in spin-orbit coupled spin-2 condensate

Pardeep Kaur\* and Sandeep Gautam†

*Department of Physics, Indian Institute of Technology Ropar, Rupnagar, Punjab 140001, India*

S. K. Adhikari‡

*Instituto de Física Teórica, Universidade Estadual Paulista - UNESP, 01.140-070 São Paulo, São Paulo, Brazil*

We study supersolid-like crystalline structures emerging in the stationary states of a quasi-two-dimensional spin-orbit (SO)-coupled spin-2 condensate in the ferromagnetic, cyclic, and antiferromagnetic phases by solving a mean-field model. Interplay of different strengths of SO coupling and interatomic interactions gives rise to a variety of non-trivial density patterns in the emergent solutions. For small SO-coupling strengths  $\gamma$  ( $\gamma \approx 0.5$ ), the ground state is an axisymmetric multi-ring soliton for polar, cyclic and weakly-ferromagnetic interactions, whereas for stronger-ferromagnetic interactions a circularly-asymmetric soliton emerges as the ground state. Depending on the values of interaction parameters, with an increase in SO-coupling strength, a stripe phase may also emerge as the ground state for polar and cyclic interactions. For intermediate values of SO-coupling strength ( $\gamma \approx 1$ ), in addition to these solitons, one could have a quasi-degenerate triangular-lattice soliton in all magnetic phases. On further increasing the SO-coupling strength ( $\gamma \gtrsim 4$ ), a square-lattice and a superstripe soliton emerge as quasi-degenerate states. The emergence of all these solitons can be inferred from a study of solutions of the single-particle Hamiltonian.

## I. INTRODUCTION

The experimental realization of spinor condensates has opened up a plethora of possibilities to explore the physics of these quantum degenerate gases [1]. As the constituent atoms of the condensates are neutral, an exciting challenge in the field of quantum degenerate gases was to introduce the spin-orbit (SO) coupling, i.e., the coupling between the spin of an atom and its linear momentum. The same was realized in experiments by creating non-abelian gauge potentials through Raman lasers which coherently couple the spin-component states of a spinor Bose-Einstein condensate (BEC) [2–5]. An SO-coupled BEC has been used as a quantum simulator to study spin-Hall effect [6], fractional topological insulators [7], and spin-current generation [8], etc. [9]. In a pseudospin-1/2 ( $F = 1/2$ ) spinor condensate with an equal-strength mixture of Rashba [10] and Dresselhaus [11] SO couplings, three ground-state phases emerge, e.g. stripe, plane-wave, and zero-momentum phases [12]. An equal-strength mixture of Rashba and Dresselhaus SO couplings has also been realised in spin-1 condensates [5] and experimental schemes to realize Rashba SO-coupled spin-1 ( $F = 1$ ) and spin-2 ( $F = 2$ ) BECs have also been proposed [13].

A vector-bright soliton is a self-bound multi-component solitary wave which maintains its shape while moving with a constant velocity. In the absence of SO coupling, in quasi-two-dimensional (quasi-2D) [14] and three-dimensional (3D) [15] settings a soliton cannot be stabilized due to a collapse instability. How-

ever, it has been theoretically demonstrated [16] that an SO-coupling leads to a stabilization of self-trapped solutions like bright solitons in quasi-2D [17] and 3D [18] spinor BECs. Vector-bright solitons have been studied extensively in SO-coupled quasi-one-dimensional (quasi-1D) [19], quasi-2D [20], and 3D pseudospin-1/2 BECs [21]. These self-trapped solitary waves have also been predicted to emerge in SO-coupled quasi-1D [22], quasi-2D [17, 23], and 3D spin-1 BECs [18]. In an SO-coupled quasi-2D spin-1 BEC, the existence of square-lattice solitons with a square-lattice modulation in the total density has also been demonstrated [23]. However, these self-trapped solitons are still unexplored in the case of quasi-2D SO-coupled spin-2 condensates and we undertake a comprehensive study of the same in this paper. A spin-2 BEC has three magnetic phases compared to two for a spin-1 BEC. The SO-coupled spin-2 BEC density is expected to exhibit more complex symmetry properties compared to the spin-1 case and the interplay of spin-independent and two spin-dependent interactions with SO coupling is expected to lead to a richer variety of emergent patterns in a spin-2 BEC [24, 25].

An exciting recent development in the field has been the experimental realization of a supersolid phase of matter in dipolar BECs, where by tuning the ratio of dipolar to contact interactions, the system first undergoes a phase transition to a supersolid phase, which is followed by a crossover to an insulating phase with a further decrease in the strength of contact interaction [26]. The excitation spectrum of the dipolar BECs in the supersolid phase has further confirmed that this phase corresponds to a simultaneous (and spontaneous) breaking of continuous translational and global gauge symmetries [27]. The existence of a supersolid-like stripe phase with both diagonal and off-diagonal orders has been observed in SO-coupled pseudospin-1/2 spinor condensates [28]. As no additional symmetry is broken vis-à-vis the system with-

\*2018phz0004@iitrpr.ac.in

†sandeep@iitrpr.ac.in

‡sk.adhikari@unesp.br, <http://www.ift.unesp.br/users/adhikari>

out Raman coupling, these supersolid-like stripes have been termed superstripes [29, 30].

In the present study, we consider a quasi-2D spin-2 condensate with a Rashba SO coupling. We investigate theoretically the self-trapped solitons of the BEC in the mean-field approximation [31, 32], wherein a spin-2 condensate is described by a set of five coupled Gross-Pitaevskii (GP) equations. We study the soliton formation for small SO-coupling strength  $\gamma$  ( $\gamma \approx 0.5$ ), for moderate SO-coupling strength ( $\gamma \approx 1$ ) and also for large SO-coupling strengths ( $\gamma \gtrsim 4$ ). For small SO-coupling strengths,  $(-2, -1, 0, +1, +2)$ -type multi-ring solitons appear in the three possible magnetic phases – ferromagnetic, anti-ferromagnetic, and cyclic – as the stationary-state solution, where the numbers in the parentheses are the phase winding numbers in components  $m_f = +2, +1, 0, -1, -2$ , respectively, in addition to circularly-asymmetric solutions. We minimize the spin-dependent-interaction energy and the SO-coupling energy to establish the allowed values of angular momentum (phase winding numbers) in different components of the system.

For moderate ( $\gamma \approx 1$ ) to strong SO-coupling strengths ( $\gamma \gtrsim 4$ ), depending on interaction parameters, multiple quasi-degenerate solitons may emerge in different magnetic phases which include triangular-lattice soliton, with hexagonal lattice formation and square-lattice soliton, with square lattice formation, in addition to stripe and superstripe solitons, all with supersolid-like properties. These states are quasi-degenerate because of internal symmetry properties. In the limit of vanishing attractive interactions, all localized solitonic states will have the same energy. The different localized quasi-degenerate solitonic states are created for a non-zero  $|c_0|$  and as  $|c_0|$  increases the degeneracy will be gradually removed. Of these different states, the triangular-lattice, square-lattice, and superstripe solitons have spatially-periodic modulation in both component and total densities, whereas the stripe soliton does not have any modulation in total density. We also construct the degenerate ground state solutions of the non-interacting SO-coupled condensate in order to anticipate the different types of solitons with supersolid-like properties, which might emerge with the introduction of interactions. We confirm the stability of these solutions by real-time simulation over long periods of time using the converged imaginary-time wave function as the initial state.

The head-on collision between two  $(-2, -1, 0, +1, +2)$ -type multi-ring solitons has also been studied. The mean-field GP equations in presence of an SO coupling are not Galilean invariant and we introduce a Galilean-transformed GP equations to study a moving soliton. We find that a moving multi-ring soliton gets deformed with the increase of velocity and ceases to exist beyond a critical velocity; so we study the collision at small velocities. At larger velocities the collision is found to be quasi elastic with the solitons passing through each other. At small velocities the collision is inelastic and the two solitons join to form a single entity and the identity of the colliding

solitons is lost.

The paper is organized as follows. In the Sec. II A, we present the mean-field GP equations of an SO-coupled spin-2 BEC. In Sec. II B, assuming a circular symmetry we establish the allowed phase-winding numbers for the system from a minimization of the interaction and SO-coupling energy terms. In Sec. II C, we demonstrate the possibility of multi-ring, stripe, square-lattice, and triangular-lattice formation from solutions of the non-interacting system. In Sec. III, we discuss a variety of self-trapped solutions emerging at different SO-coupling strengths from a numerical solution of the GP equations. In Sec. III A, we show that axisymmetric multi-ring and circularly-asymmetric solitons, the latter for ferromagnetic BECs, are possible for small SO-coupling strengths  $\gamma$ . In Sec. III B, we demonstrate that quasi-degenerate axisymmetric multi-ring and triangular-lattice solitons emerge for medium values of  $\gamma$ . In Sec. III C, we establish the formation of multi-ring, square-lattice, superstripe and stripe solitons for large  $\gamma$ . We confirm the dynamic stability of the different solitons using real-time evolution with the addition of a small random noise to the order parameter in Sec. III D. The bifurcation behaviour is discussed in Sec. III E. The Galilean transformed mean-field model for the condensate is introduced in Sec. III F, which we use to study the moving solitons and collisions between them.

## II. MEAN FIELD MODEL FOR SPIN-ORBIT-COUPLED SPIN-2 BEC

### A. Gross-Pitaevskii equations

We consider an SO-coupled spin-2 spinor BEC free in the  $x$ - $y$  plane and confined by a harmonic trap  $V(\mathbf{r}) = m\omega_z^2 z^2/2$  along the  $z$ -direction to its Gaussian ground state. The trapping frequency  $\omega_z$  is strong enough to freeze the dynamics along  $z$  direction. The single-particle Hamiltonian of this system in the presence of Rashba SO coupling is given by [33]

$$H_0 = \frac{p_x^2 + p_y^2}{2m} + \gamma(p_y S_x - p_x S_y), \quad (1)$$

where  $p_x = -i\hbar\partial_x \equiv -i\hbar\partial/\partial x$  and  $p_y = -i\hbar\partial_y \equiv -i\hbar\partial/\partial y$  are the momentum operators along  $x$  and  $y$  axes, respectively,  $\gamma$  is the strength of SO coupling,  $S_x$  and  $S_y$  are the irreducible representations of the  $x$  and  $y$  components of angular momentum operators for spin-2 particle, respectively. The  $(j', j)$ th element of these  $5 \times 5$  matrices are

$$(S_x)_{j',j} = \frac{1}{2} \left( \sqrt{(2-j)(2+j+1)}\hbar\delta_{j',j+1} + \sqrt{(2+j)(2-j+1)}\hbar\delta_{j',j-1} \right), \quad (2)$$

$$(S_y)_{j',j} = -\frac{1}{2}i \left( \sqrt{(2-j)(2+j+1)}\hbar\delta_{j',j+1} - \sqrt{(2+j)(2-j+1)}\hbar\delta_{j',j-1} \right), \quad (3)$$

where  $j'$  and  $j$  represent the spin projections  $m_f$  and can have values  $\pm 2, \pm 1, 0$ .

The reduced quasi-2D spinor BEC can be described by a set of five coupled mean-field partial differential GP equations for the wave-function components  $\phi_j$  and are given in dimensionless form as [1]

$$i\partial_t \phi_{\pm 2} = \mathcal{H}\phi_{\pm 2} + c_0 \rho \phi_{\pm 2} + c_1 (F_{\mp} \phi_{\pm 1} \pm 2F_z \phi_{\pm 2}) + c_2 \frac{1}{\sqrt{5}} \Theta \phi_{\mp 2}^* + \Gamma_{\pm 2}, \quad (4a)$$

$$i\partial_t \phi_{\pm 1} = \mathcal{H}\phi_{\pm 1} + c_0 \rho \phi_{\pm 1} + c_1 \left( \sqrt{\frac{3}{2}} F_{\mp} \phi_0 + F_{\pm} \phi_{\pm 2} \pm F_z \phi_{\pm 1} \right) - c_2 \frac{1}{\sqrt{5}} \Theta \phi_{\mp 1}^* + \Gamma_{\pm 1}, \quad (4b)$$

$$i\partial_t \phi_0 = \mathcal{H}\phi_0 + c_0 \rho \phi_0 + c_1 \sqrt{\frac{3}{2}} (F_- \phi_{-1} + F_+ \phi_{+1}) + c_2 \frac{1}{\sqrt{5}} \Theta \phi_0^* + \Gamma_0, \quad (4c)$$

where

$$\mathcal{H} = -\frac{1}{2} (\partial_x^2 + \partial_y^2),$$

$$\Theta = \frac{1}{\sqrt{5}} (2\phi_{+2}\phi_{-2} - 2\phi_{+1}\phi_{-1} + \phi_0^2), \quad F_z = \sum_j j |\phi_j|^2,$$

$$F_{\pm} = F_x \pm iF_y, \quad |\mathbf{F}|^2 = F_x^2 + F_y^2 + F_z^2 \equiv F_+ F_- + F_z^2,$$

where  $\partial_t \equiv \partial/\partial t$ ,  $\rho_j(x, y) = |\phi_j(x, y)|^2$  are component densities and  $\rho(x, y) \equiv \sum_j \rho_j(x, y)$  is the total density,  $F_{\pm} = F_x \pm iF_y$ ,  $|\mathbf{F}|^2 = F_x^2 + F_y^2 + F_z^2 \equiv F_+ F_- + F_z^2$ , where  $F_x, F_y, F_z$  are the three components of the spin-density vector  $\mathbf{F}$ , and  $\Theta$  is the spin-singlet pair amplitude. In Eqs. (4a)-(4c), the interaction parameters and SO coupling terms are defined as

$$c_0 = \frac{2\sqrt{2\pi}N(4a_2 + 3a_4)}{7a_{\text{osc}}}, \quad c_1 = \frac{2\sqrt{2\pi}N(a_4 - a_2)}{7a_{\text{osc}}}, \quad (5a)$$

$$c_2 = \frac{2\sqrt{2\pi}N(7a_0 - 10a_2 + 3a_4)}{7a_{\text{osc}}} \quad (5b)$$

$$\Gamma_{\pm 2} = -i\gamma (\partial_y \pm i\partial_x) \phi_{\pm 1}, \quad (5c)$$

$$\Gamma_{\pm 1} = -i\sqrt{\frac{3}{2}}\gamma (\partial_y \pm i\partial_x) \phi_0 - i\gamma (\partial_y \mp i\partial_x) \phi_{\pm 2}, \quad (5d)$$

$$\Gamma_0 = -i\sqrt{\frac{3}{2}}\gamma [(\partial_y - i\partial_x)\phi_{+1} + (\partial_y + i\partial_x)\phi_{-1}], \quad (5e)$$

where  $a_0, a_2$ , and  $a_4$  are  $s$ -wave scattering lengths in the possible total spin channels 0, 2 and 4, respectively, for a spin-2 BEC, and  $N$  is the total number of bosons.

In this study we will consider a self-attractive ( $c_0 < 0$ ) system. Depending on the values of  $c_1$  and  $c_2$  we can have three magnetic phases [1] – ferromagnetic, anti-ferromagnetic, and cyclic – as illustrated in Fig. 1. The units of length, density, time, and energy considered in Eqs. (4a)-(4c) are oscillator length  $a_{\text{osc}} = \sqrt{\hbar/m\omega_z}$ ,  $a_{\text{osc}}^{-2}$ ,  $\omega_z^{-1}$ , and  $\hbar\omega_z$ , respectively. The dimensionless formulation of mean-field model for the condensate has the normalization condition  $\int \rho(x, y) dx dy = 1$ . The number of

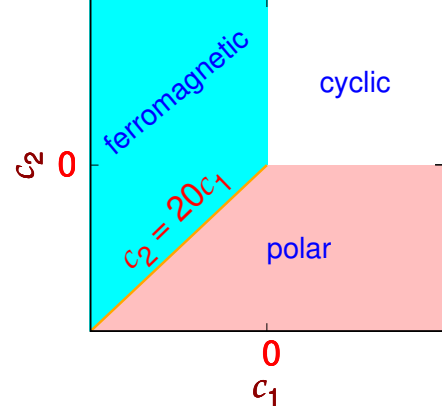


FIG. 1: (Color online) The  $c_2$  versus  $c_1$  phase plot (not to scale) illustrating ferromagnetic, anti-ferromagnetic, and cyclic phases in the absence of SO coupling. All the figures in this work are plotted in dimensionless units.

particles along with energy

$$E = \int dx dy \left[ \sum_{j=-2}^{+2} \phi_j^* \mathcal{H} \phi_j + \frac{1}{2} c_0 \rho^2 + \frac{1}{2} c_1 |\mathbf{F}|^2 + \frac{1}{2} c_2 |\Theta|^2 + \sum_{j=-2}^{+2} \phi_j^* \Gamma_j \right], \quad (6)$$

are two conserved quantities of an SO-coupled BEC. In the presence of SO-coupling ( $\gamma \neq 0$ ), magnetization ( $\equiv \int F_z dx dy = \int dx dy [2\rho_{+2}(x, y) - 2\rho_{-2}(x, y) + \rho_{+1}(x, y) - \rho_{-1}(x, y)]$ ) is not a conserved quantity, although it is conserved for  $\gamma = 0$ .

## B. Phase Requirement

The permitted vortex configurations in a spinor BEC depend on the inter-component phase relationships. Considering a circular symmetry, the spinor order parameter for a vortex configuration in circular polar co-ordinates  $(r, \theta)$  can be written in terms of amplitude and phase part as

$$\phi_j(r, \theta) = R_j(r) e^{i(w_j \theta + \alpha_j)}, \quad (7)$$

where  $R_j = |\phi_j(r, \theta)| \geq 0$  and  $j = 0, \pm 1, \pm 2$ . The phases of the component wave functions have contributions from winding number  $w_j$  of the phase-singularity which is an integer and any other constant phase  $\alpha_j$ . Using the *ansatz* (7), one can minimize the interaction and the energy contribution from the SO coupling leading to following independent relationships among the permitted winding numbers (details are given in Appendix):

$$w_{+2} - w_{+1} + 1 = 0, \quad w_{+1} - w_0 + 1 = 0, \quad (8a)$$

$$w_{-2} - w_{-1} - 1 = 0, \quad w_{-1} - w_0 - 1 = 0. \quad (8b)$$

The allowed winding-number combinations are  $(-2, -1, 0, +1, +2)$ ,  $(-1, 0, +1, +2, +3)$ ,

(0, +1, +2, +3, +4), and higher. It is to be also noted that an axisymmetric configuration without any phase singularity in any of the components, i.e., with a winding number combination of (0,0,0,0,0), is not allowed as per Eqs. (8a)-(8b). Using Eq. (7), kinetic energy (KE) of the condensate is

$$\text{KE} = \sum_{j=-2}^2 w_j^2 \int \frac{\pi \phi_j^2}{r} dr, \quad (9)$$

which indicates that the system might end up favoring small winding numbers.

### C. Single-Particle Hamiltonian

The emergence of the axisymmetric solutions to Eqs. (4a)-(4c) in the form of a  $(-2, -1, 0, +1, +2)$ -type multi-ring state can be inferred from the eigenfunction of the single-particle (or non-interacting) Hamiltonian in Eq. (1). One eigenfunction of the single-particle Hamiltonian with (minimum) energy  $-2\gamma^2$  is

$$\Phi = \frac{1}{4} \begin{pmatrix} e^{-2i\varphi} \\ -2e^{-i\varphi} \\ \sqrt{6} \\ -2e^{i\varphi} \\ e^{2i\varphi} \end{pmatrix} e^{ik_x x + i y k_y} \equiv \zeta(\varphi) e^{ik_x x + i y k_y}, \quad (10)$$

where  $\varphi = \tan^{-1}(k_y/k_x)$  and  $k^2 = k_x^2 + k_y^2 = (2\gamma)^2$  which corresponds to the minimum of eigen energy

$$E(k_x, k_y) = \frac{1}{2} \left( k_x^2 + k_y^2 - 4\gamma \sqrt{k_x^2 + k_y^2} \right). \quad (11)$$

The two-dimensional contour plot of eigen energy  $E(k_x, k_y)$  for  $\gamma = 1$  is shown in Fig. 2. The eigen energy is minimum along a circle of radius 2, i.e., for  $k_x^2 + k_y^2 = 4$ . Hence a typical  $\mathbf{k} \equiv (k_x, k_y)$  which minimizes the eigen energy is as shown in Fig. 2, where  $\varphi$  can vary from 0 to  $2\pi$ . The eigenfunctions with different orientations of the vector  $\mathbf{k} \equiv \{k_x, k_y\}$  in the  $k_x - k_y$  plane, as shown in Fig. 2, are all degenerate. Thus a most general solution to the single-particle Hamiltonian can be obtained by considering the superposition of eigenfunctions (10) with  $\mathbf{k}$  allowed to point along all directions in 2D plane. The generic solution, so obtained, is

$$\begin{aligned} \Phi_{\text{MR}} &= \frac{1}{8\pi} \int_0^{2\pi} \begin{pmatrix} e^{-2i\varphi} \\ -2e^{-i\varphi} \\ \sqrt{6} \\ -2e^{i\varphi} \\ e^{2i\varphi} \end{pmatrix} e^{i2\gamma r \cos(\varphi-\theta)} d\varphi, \quad (12) \\ &= \frac{1}{4} \begin{pmatrix} -e^{-2i\theta} J_2(2\gamma r) \\ -2ie^{-i\theta} J_1(2\gamma r) \\ \sqrt{6} J_0(2\gamma r) \\ -2ie^{i\theta} J_1(2\gamma r) \\ -e^{2i\theta} J_2(2\gamma r) \end{pmatrix}, \quad (13) \end{aligned}$$

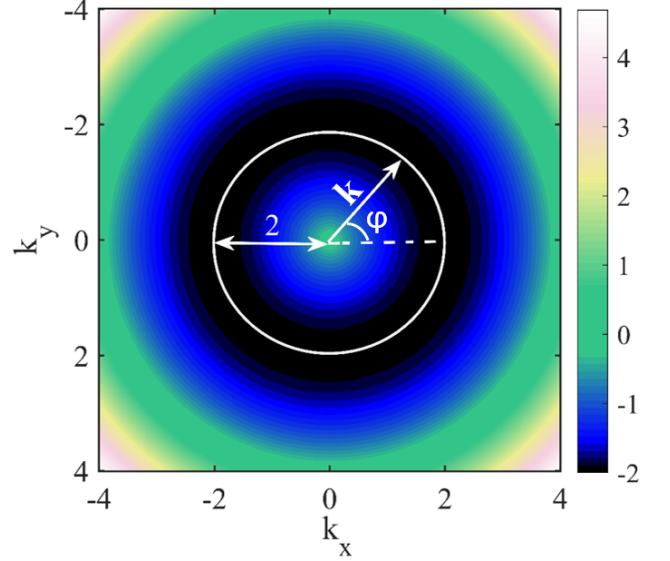


FIG. 2: (Color online) Contour plot of eigen energy  $E(k_x, k_y)$  in Eq. (11) for  $\gamma = 1$ . The minima corresponding to  $k_x^2 + k_y^2 = 4$  is a circle of radius 2. A typical  $\mathbf{k}$  with magnitude 2 and oriented at a polar angle  $\varphi$  is also shown.

where  $\theta = \tan^{-1} y/x$ , and  $J_n(2\gamma r)$  with  $n = 0, 1, 2$  is the Bessel function of first kind of order  $n$  and where  $\Phi_{\text{MR}}$  has the phase singularities of a multi-ring (MR) soliton. Solution (13) agrees with the permissible winding number combination of  $(-2, -1, 0, +1, +2)$  obtained earlier based on energetic considerations, viz. Eq.(8), and corresponds to a  $(-2, -1, 0, +1, +2)$ -type multi-ring soliton. As the component densities,  $\rho_j \sim |J_j|^2$ , the densities would have a long undulating tail, and in the asymptotic region with  $r \rightarrow \infty$ ,  $\rho_j \sim \sqrt{2/(2\pi\gamma r)} \cos(2\gamma r - \pi|j|/2 - \pi/4)$ .

Besides superposition of an infinite number of plane waves, viz. Eq. 12, one can also have a superposition of (a) two counter-propagating plane waves, (b) three plane waves whose propagation vectors make an angle  $2\pi/3$  with each other, or (c) four plane waves whose propagation vectors make an angle  $\pi/2$  with each other. Choosing  $x$ -direction as the direction for one of these wave vectors, these superpositions, representing a stripe (ST), triangular lattice (TL), and square lattice (SL), respectively, are

$$\Phi_{\text{ST}} = \frac{1}{\sqrt{2}} [\zeta(0)e^{i2\gamma x} + \zeta(\pi)e^{-i2\gamma x}], \quad (14a)$$

$$\begin{aligned} \Phi_{\text{TL}} &= \frac{1}{\sqrt{3}} [\zeta(0)e^{i2\gamma x} + \zeta(2\pi/3)e^{i(-\gamma x + \gamma\sqrt{3}y)} \\ &\quad + \zeta(4\pi/3)e^{i(-\gamma x - \gamma\sqrt{3}y)}], \quad (14b) \end{aligned}$$

$$\begin{aligned} \Phi_{\text{SL}} &= \frac{1}{2} [\zeta(0)e^{i2\gamma x} + \zeta(\pi/2)e^{i2\gamma y} + \zeta(\pi)e^{-i2\gamma x} \\ &\quad + \zeta(3\pi/2)e^{-i2\gamma y}]. \quad (14c) \end{aligned}$$

The component densities and corresponding total density for these degenerate solutions corresponding to  $|\Phi_{\text{ST}}|^2$ ,  $|\Phi_{\text{TL}}|^2$ ,  $|\Phi_{\text{SL}}|^2$  and  $|\Phi_{\text{MR}}|^2$ , are shown in Figs.

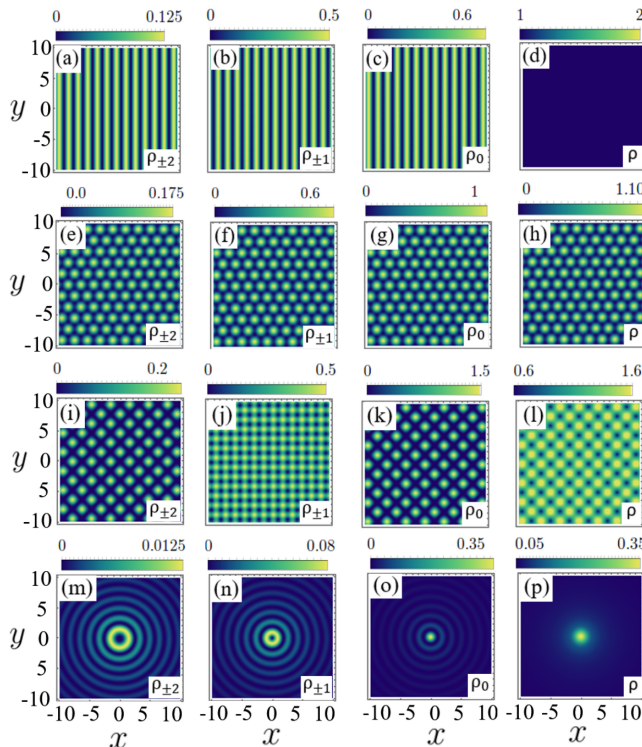


FIG. 3: (Color online) The two-dimensional contour plot of densities of the components  $j = \pm 2$ ,  $j = \pm 1$ ,  $j = 0$ , and total density corresponding to  $\Phi_{ST}$  is shown in (a)-(d) for SO-coupling strength  $\gamma = 1$ . The same for  $\Phi_{TL}$ ,  $\Phi_{SL}$  and  $\Phi_{MR}$  are shown in (e)-(h), (i)-(l) and (m)-(p), respectively.

3(a)-(d), 3(e)-(h), 3(i)-(l), and 3(m)-(p), respectively. If one examines the total density corresponding to these superpositions in Eqs. (13)-(14) as plotted in Figs. 3(d), (h), (l), and (p), then in the total density corresponding to  $|\Phi_{MR}|^2$  and  $|\Phi_{ST}|^2$  there is no spatially-periodic modulation, whereas the total density  $|\Phi_{TL}|^2$  and  $|\Phi_{SL}|^2$  will have a hexagonal and a square-lattice crystallization, respectively. The localized solitons studied in this paper can be qualitatively approximated by the single-particle solutions (13)-(14) multiplied by a localized Gaussian function. In the numerical solution by an imaginary-time propagation such approximations can be used as the initial functions for different solitons with appropriate symmetry.

### III. NUMERICAL RESULTS

We numerically solve the GP equations (4a)-(4c) using split time-step Fourier spectral method [34]. For SOC strengths upto  $\gamma = 1$ , we consider the spatial step sizes  $\Delta x = \Delta y = 0.1$ . Here the two-dimensional box size for solving the GP equations is  $60 \times 60$ . For  $\gamma > 1$ , the step sizes and box size considered are  $\Delta x = \Delta y = 0.05$ ,  $\Delta t = 0.00025$  and  $40 \times 40$ , respectively. The time steps for

imaginary- and real-time propagation are  $\Delta t = 0.1 \times \Delta x^2$  and  $\Delta t = 0.05 \times \Delta x^2$ , respectively. The imaginary-time propagation method is used for finding the lowest-energy state of a specific symmetry, whereas real-time propagation is used to study the dynamics. The initial guess for order parameter to obtain the stripe, triangular-lattice and square-lattice solitons are considered as solutions to non-interacting condensate, viz. Eqs. (14a)-(14c), multiplied by a localized Gaussian state and the same for the multi-ring soliton is a two-dimensional Gaussian function with appropriate vortices phase-imprinted on different components. As magnetization is not conserved, during time propagation magnetization is allowed to evolve freely and attain a final converged value independent of the magnetization of the initial state. The dynamic stability of the solutions is demonstrated by real-time evolution with a small random noise added to the order parameter at  $t = 0$ , wherein they retain their structure over long periods of evolution.

Our numerical studies reveal that an SO-coupled spin-2 BEC with attractive interactions can have a variety of self-trapped stationary solutions including the cases where the total density of the condensate exhibits regular hexagonal or square patterns. The ground-state phase diagram of a ferromagnetic BEC with  $c_0 = -0.5$ ,  $c_1 = -0.025$  and polar and cyclic BECs with  $c_0 = -0.5$ ,  $c_1 = 0.025$  in  $c_2$ - $\gamma$  planes are shown in Figs. 4(a) and (b), respectively. For the ferromagnetic BEC, as the strength of the SO coupling is increased, the ground state changes from an axisymmetric multi-ring soliton to an asymmetric soliton. For the polar and cyclic BECs, the ground-state phase changes from a multi-ring soliton to a stripe soliton above a critical SO-coupling for the chosen set of interaction parameters. In a narrow strip near  $\gamma = 1$ , a triangular-lattice soliton appears as one of the quasi-degenerate ground states in all three magnetic phases as shown by shaded regions in Figs. 4(a) and (b). It is also pertinent to point out that the energy difference among the quasi-degenerate states decreases (increases) with a decrease (increase) in  $|c_0|$ .

#### A. Small SO-coupling strength

##### 1. Ferromagnetic Phase

In an SO-coupled spin-2 BEC with  $c_0 < 0$ ,  $c_1^{(1)} \leq c_1 < 0$ , and  $c_2 > 0$ , which implies that the system is weakly ferromagnetic, where  $c_1^{(1)}$  is a constant, viz. Fig. 1, the lowest-energy state has an axisymmetric density pattern corresponding to a  $(-2, -1, 0, +1, +2)$ -type multi-ring soliton, whereas the higher energy states could be axisymmetric or circularly asymmetric. For smaller  $c_1$ , i.e.  $c_1 < c_1^{(1)}$ , the interactions become (relatively) strongly ferromagnetic, and the ground state corresponds to a circularly-asymmetric soliton. The  $(-2, -1, 0, +1, +2)$ -type axisymmetric multi-ring soliton continues to exist



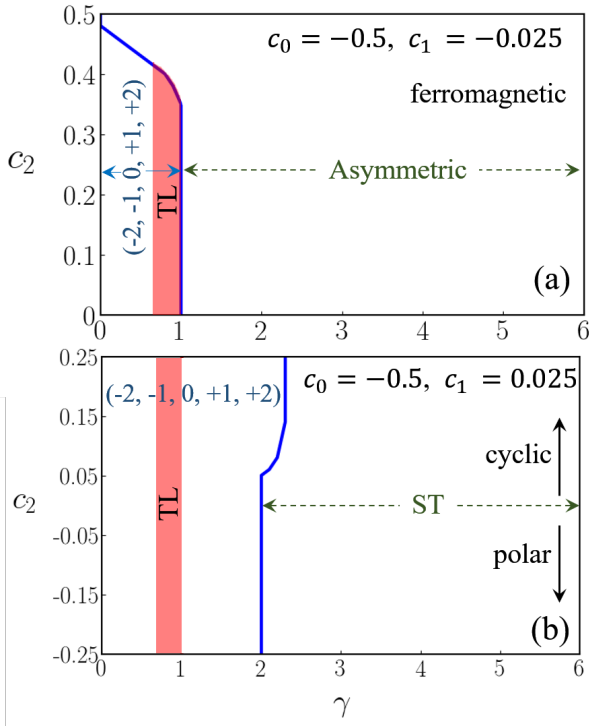


FIG. 4: (Color online) The  $c_2$  versus  $\gamma$  phase plots for the ground states are shown (a) for the ferromagnetic phase with  $c_0 = -0.5$  and  $c_1 = -0.025$  and (b) for the cyclic and polar phases with  $c_0 = -0.5$  and  $c_1 = 0.025$ . In (a) for small SO-coupling strengths, the axisymmetric  $(-2, -1, 0, +1, +2)$  state is the ground state similar to the state shown in 5(a)-(d), whereas for larger SO-coupling strengths, the asymmetric soliton state is the ground state similar to the state shown in 6(f)-(j). In (b) for small SO-coupling strengths, the axisymmetric  $(-2, -1, 0, +1, +2)$  state is the ground state similar to the state shown in 5(a)-(d), whereas for larger SO-coupling strengths, the stripe soliton state (ST) is the ground state similar to the state shown in 9(a)-(d). Difference in energy of other quasi-degenerate solitons from these ground states is  $\gtrsim 10^{-4}$ . As an illustration, one of the quasi-degenerate states is the triangular-lattice (TL) state similar to the state shown in 7(a)-(d), which occupies a narrow region near  $\gamma = 1$  and is shown by a red shaded strip. The energy differences between the triangular lattice (TL) state and the  $(-2, -1, 0, +1, +2)$ -type multi-ring ground state in plots (a) and (b) are  $10^{-4}$ - $10^{-3}$ .

in this case, but is no longer the ground state. With further decrease of  $c_1$  below another constant  $c_1^{(2)}$  an increase of attractive interaction leads to a collapse of the condensate and no solution exists. The explicit values of the constants  $c_1^{(1)}$  and  $c_1^{(2)}$  are dependent on the parameters  $c_0$ ,  $c_2$  and  $\gamma$ .

*Axisymmetric multi-ring soliton:* As an example in the ferromagnetic phase, we consider  $c_0 = -0.5$ ,  $c_1 = -0.025 > c_1^{(1)} = -0.05$ ,  $c_2 = 0.25$  and  $\gamma = 0.5$ . The ground state solution for this set of parameters is an axisymmetric  $(-2, -1, 0, +1, +2)$ -type multi-ring soliton

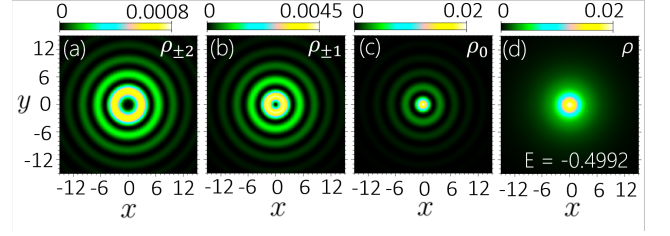


FIG. 5: (Color online) Contour plot of density of the components (a)  $j = \pm 2$ , (b)  $j = \pm 1$ , (c)  $j = 0$ , and (d) total density of an axisymmetric  $(-2, -1, 0, +1, +2)$ -type multi-ring soliton with  $c_0 = -0.5$ ,  $c_1 = -0.025$ ,  $c_2 = 0.25$ , (ferromagnetic phase) and  $\gamma = 0.5$  with energy  $E = -0.4992$ .

with energy  $E = -0.4992$  as exhibited in Fig. (5) through a contour plot of the component densities (a)  $\rho_{\pm 2}$ , (b)  $\rho_{\pm 1}$ , (c)  $\rho_0$  and (d) the total density  $\rho$ . The densities of components  $\pm j$  with  $j = 1, 2$  are equal. This state has the same rotational symmetry as the ground state of the non-interacting SO-coupled condensate governed by Eq. (13) and has a long undulating tail of decreasing amplitude consistent with the asymptotic behaviour of Bessel functions. If the wave function (13) is multiplied by a localized Gaussian function, the resultant function qualitatively produces the density of the state displayed in Fig. 5. Hence the density and symmetry properties of the actual physical state can be inferred from a study of the eigenfunctions of the single-particle Hamiltonian. The total density has no core at the center as the vortex cores of  $j = \pm 2$ , and  $j = \pm 1$  components are filled by a non-zero density at the center of the  $j = 0$  component. The first zeros of  $J_0(r)$ ,  $J_1(r)$ , and  $J_2(r)$  are 2.40483, 3.83171, and 5.13562, respectively, and these agree very well with the results presented in Fig. (5). Numerically, this solution is obtained by evolving Eqs. (4a)-(4c) in imaginary time and using, as an initial guess, a two-dimensional Gaussian function multiplied by an appropriate phase factor of  $\exp(-ij\varphi)$  for the  $j$ th component. For the same set of parameters, we also have a  $(-1, 0, +1, +2, +3)$ -type multi-ring soliton with an energy -0.4991 as shown in Fig. 6(a)-(e) through a contour plot of component densities (a)  $\rho_{+2}$ , (b)  $\rho_{+1}$ , (c)  $\rho_0$ , (d)  $\rho_{-1}$ , and (e)  $\rho_{-2}$ . The quasi-degeneracy between the two solutions shown in Figs. 5(a)-(d) and 6(a)-(e) is lifted with an increase in  $|c_0|$ . The winding number combinations for these axisymmetric solutions are in accordance with relations given in Eq. (8).

*Circularly-asymmetric soliton:* By considering the parameters in the (relatively) strongly ferromagnetic phase with  $c_0 = -0.5$ ,  $c_1 = -0.1$ ,  $c_2 = 0.25$  and  $\gamma = 0.5$ , the circularly-asymmetric soliton displayed in Figs. 6(f)-(j) through a contour plot of component densities turns out to be the ground state while the axisymmetric  $(-2, -1, 0, +1, +2)$ -type multi-ring soliton appears as an excited state. Asymmetry of the solution arises, in this case, as different from the  $(-2, -1, 0, +1, +2)$ -type soli-

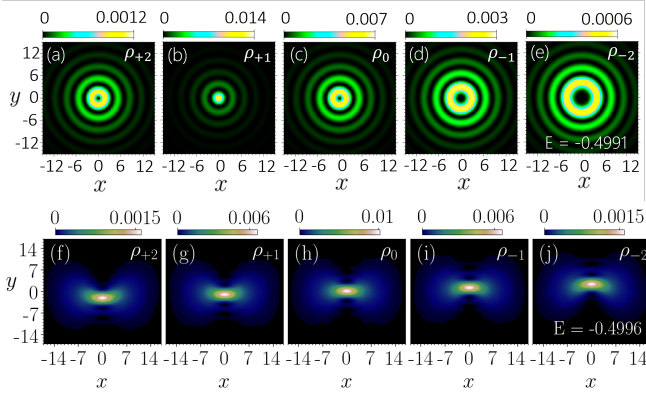


FIG. 6: (Color online) Contour plot of density of components (a)  $j = +2$ , (b)  $j = +1$ , (c)  $j = 0$ , (d)  $j = -1$ , and (e)  $j = -2$  of an axisymmetric  $(-1, 0, +1, +2, +3)$ -type multi-ring soliton with  $c_0 = -0.5$ ,  $c_1 = -0.025$ ,  $c_2 = 0.25$ , (ferromagnetic phase)  $\gamma = 0.5$  and energy  $E = -0.4991$ ; the same of a circularly-asymmetric soliton with  $c_0 = -0.5$ ,  $c_1 = -0.1$ ,  $c_2 = 0.25$ , (strongly ferromagnetic phase),  $\gamma = 0.5$ , and energy  $E = -0.4996$  in (f)-(j)..

ton displayed in Figs. 5(a)-(d), the phase-singularities in  $\pm j$  components of the circularly-asymmetric soliton exhibited in Figs. 6(f)-(j) do not overlap. When we keep on decreasing  $c_1$  further, then these singularities in  $\pm j$  components move further apart along  $y$ -axis. For  $c_0 = -0.5$ ,  $c_1 = -1.3$ ,  $c_2 = 0.25$  and  $\gamma = 0.5$ , phase-singularities lie in the region where the condensate density is quite small (not shown here) and hence no perceptible density hole is visible in the component densities  $\rho_j$ . If we decrease  $c_1$  below  $c_1^{(2)} = -1.3$ , while keeping  $c_0$ ,  $c_2$ , and  $\gamma$  fixed, then the condensate collapses.

## 2. Cyclic and Polar phases

For small SO-coupling strengths, in both cyclic and polar phases, similar to the ferromagnetic phase, the axisymmetric  $(-2, -1, 0, +1, +2)$ -type multi-ring soliton emerges as the ground state, whereas the axisymmetric  $(-1, 0, +1, +2, +3)$ -type soliton appears as a metastable state (result not shown here). For example, with  $c_0 = -0.5$ ,  $c_1 = 0.025$ ,  $c_2 = 0.25$  and  $\gamma = 0.5$  corresponding to the cyclic phase, viz. Fig. 1, the axisymmetric  $(-2, -1, 0, +1, +2)$ -type and  $(-1, 0, +1, +2, +3)$ -type multi-ring solitons have energies  $-0.4992$  and  $-0.3864$ , respectively. Similarly, with  $c_0 = -0.5$ ,  $c_1 = 0.025$ ,  $c_2 = -0.25$  and  $\gamma = 0.5$ , corresponding to the polar phase, the respective energies of axisymmetric  $(-2, -1, 0, +1, +2)$ -type and  $(-1, 0, +1, +2, +3)$ -type multi-ring solitons are  $-0.4994$  and  $-0.3855$ . In both cases, the  $(-2, -1, 0, +1, +2)$ -type multi-ring soliton is the ground state.

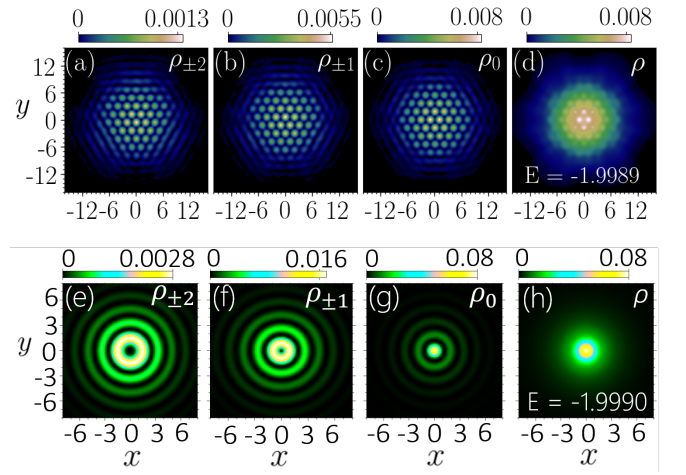


FIG. 7: (Color online) Contour plot of density of components (a)  $j = \pm 2$ , (b)  $j = \pm 1$ , (c)  $j = 0$ , and (d) total density of a triangular-lattice soliton with  $c_0 = -0.5$ ,  $c_1 = 0.025$ ,  $c_2 = 0.25$ , (cyclic phase)  $\gamma = 1$ , and energy  $E = -1.9989$ ; the same of a  $(-2, -1, 0, +1, +2)$ -type multi-ring soliton for the same parameters and  $E = -1.9990$  in (e)-(h).

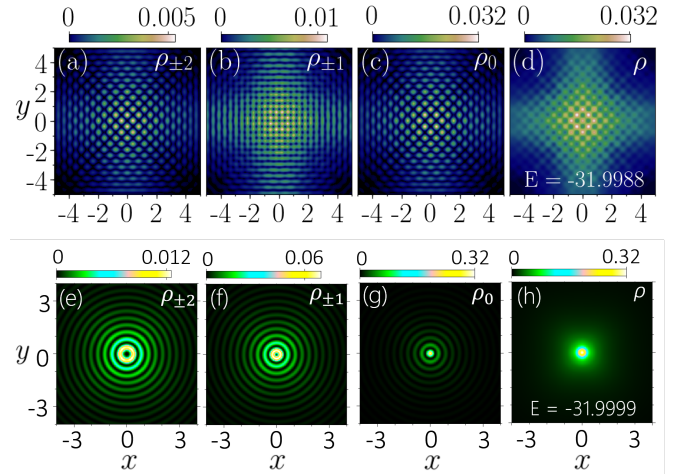


FIG. 8: (Color online) Contour plot of density of a square-lattice soliton of components (a)  $j = \pm 2$ , (b)  $j = \pm 1$ , (c)  $j = 0$  and (d) total density for  $c_0 = -0.5$ ,  $c_1 = -0.025$ ,  $c_2 = 0.25$ , (ferromagnetic phase)  $\gamma = 4$  and  $E = -31.9988$ ; for the same parameters, the component and total densities of a  $(-2, -1, 0, +1, +2)$ -type multi-ring soliton in (e)-(h) with  $E = -31.9999$ .

## B. Intermediate SO-coupling strength

For intermediate SO-coupling strengths, we get a triangular-lattice soliton, with a hexagonal-lattice crystallization in components and total densities, in all three magnetic phases – ferromagnetic, polar and cyclic. Although a square-lattice soliton has been earlier identified in Ref. [23], a triangular-lattice soliton was not found

in the spin-1 case. For example, in the cyclic phase with  $c_0 = -0.5$ ,  $c_1 = 0.025$ ,  $c_2 = 0.25$  and  $\gamma = 1$ , the triangular-lattice soliton is shown in Fig. 7 through a contour density plot of component densities (a)  $\rho_{\pm 2}$ , (b)  $\rho_{\pm 1}$ , (c)  $\rho_0$  and (d) total density. The triangular-lattice structure is a result of superposition of three plane waves and corresponds to a solution of the non-interacting system given by Eq. (14b). However, to get a localized hexagonal structure as in Figs. 7(a)-(d), the function (14b) has to be multiplied by a localized Gaussian function. For the same parameters, an axisymmetric  $(-2, -1, 0, +1, +2)$ -type multi-ring soliton corresponding to the single-particle solution (13) is also a solution as illustrated in Figs. 7(e)-(h). Both these states, the multi-ring and the triangular-lattice solitons, have approximately the same numerical energy ( $E = -1.9990$  and  $E = -1.9989$ ) and are quasi-degenerate. This degeneracy between the two solutions is removed with an increase in  $|c_0|$  resulting in the  $(-2, -1, 0, +1, +2)$ -type multi-ring soliton as the ground state.

### C. Large SOC strength

When  $\gamma$  is increased further, different types of degenerate states appear with approximately the same energy in the three different magnetic phases. As an example, in the ferromagnetic phase with  $c_0 = -0.5$ ,  $c_1 = -0.025$ ,  $c_2 = 0.25$ , and  $\gamma \gtrsim 4$ , we get the following five types of quasi-degenerate solitons: (1) a square-lattice soliton, where as shown in Figs. 8(a)-(d), the component as well as the total densities show square-lattice crystallization consistent with the single-particle order parameter (14c), (2) a  $(-2, -1, 0, +1, +2)$ -type multi-ring soliton, corresponding to the single-particle order parameter (13), as shown in Figs. 8(e)-(h), (3) a circularly-asymmetric soliton, (4) a stripe soliton with stripe modulation in component densities corresponding to the single-particle order parameter (14)(a), and (5) a superstripe soliton which has stripe patterns in component densities  $\rho_{\pm 1}$  and square-lattice crystallization in component densities  $\rho_{\pm 2}$  and  $\rho_0$  and also total density. The three latter solitons are not shown here. In case of the square-lattice soliton, viz. Fig. 8(a)-(d), the square-lattice crystallization in components  $j = \pm 2$  and 0 are quite similar, whereas the square-lattice pattern in the components  $j = \pm 1$  is different. The lattice in components  $j = \pm 2$  and 0 makes an angle of  $45^\circ$  with the lattice in component  $j = \pm 1$  and this is consistent with density pattern corresponding to  $\Phi_{\text{SL}}$  as shown in Figs. 3(i)-(l). The prominent square lattice in total density has the same alignment as in components  $j = \pm 2$  and 0. A similar square-lattice soliton was predicted in an SO-coupled spin-1 spinor BEC [23]. The densities of components  $j = \pm 2$  and 0 ( $j = \pm 1$ ) of the square-lattice soliton of Figs. 8(a)-(d) are quite similar to the densities of components  $j = \pm 1$  ( $j = 0$ ) of the same in an SO-coupled spin-1 spinor BEC [23]; the total densities in the two cases are also quite similar. The

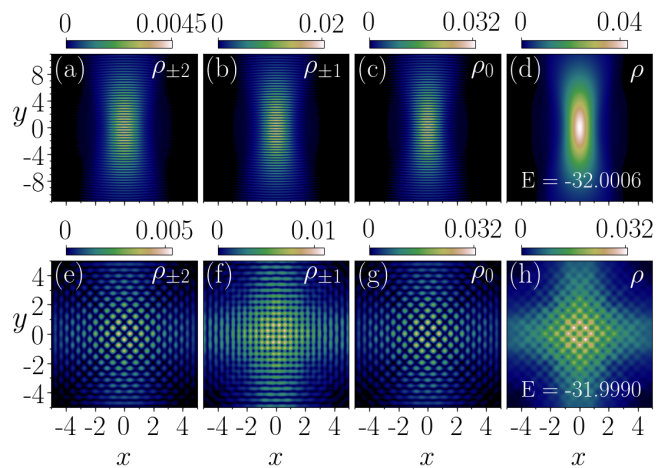


FIG. 9: (Color online) Contour plot of density of a stripe soliton of components (a)  $j = \pm 2$ , (b)  $j = \pm 1$ , (c)  $j = 0$ , and (d) total density with  $c_0 = -0.5$ ,  $c_1 = 0.025$ ,  $c_2 = 0.25$ , (cyclic phase)  $\gamma = 4$ ,  $E = -32.0006$ ; the same of a square-lattice soliton for the same parameters in (e)-(h) with  $E = -31.9990$ .

energies of these five different types of solitons are, respectively,  $-31.9988$ ,  $-31.9999$ ,  $-32.0071$ ,  $-31.9998$ , and  $-32.0020$  and hence these solitons are quasi-degenerate.

In the cyclic phase, with  $c_0 = -0.5$ ,  $c_1 = 0.025$ ,  $c_2 = 0.25$ , and  $\gamma \gtrsim 4$ , we again obtain four of the aforementioned quasi-degenerate solitons except the circularly-asymmetric soliton. The component and total densities corresponding to stripe soliton and square-lattice soliton are shown in Figs. 9(a)-(d) and 9(e)-(h), respectively. The stripe soliton of Figs. 9(a)-(d) is quite similar to the one in an SO-coupled spin-1 spinor BEC [23] for  $\gamma = 4$  in both ferromagnetic and polar phases. In both cases the stripe pattern appears only in the component densities with the total density showing no modulation. The respective energies of the stripe and the square-lattice solitons are  $-32.0006$  and  $-31.9990$ . The superstripe soliton with energy  $-32.0002$  and multi-ring soliton with energy  $-31.9999$  are not shown here.

In the polar phase, with  $c_0 = -0.5$ ,  $c_1 = 0.025$ ,  $c_2 = -0.25$ , and  $\gamma \gtrsim 4$ , we get the same four quasi-degenerate solitons as in the cyclic phase discussed above. Two of these, square-lattice soliton with energy  $-31.9987$  and superstripe soliton with energy  $-32.0023$  are shown in Figs. 10(a)-(d) and (e)-(h), respectively. The superstripe soliton has a square-lattice type spatial modulation superposed on stripes in components  $j = \pm 2$  and 0 and a stripe modulation in component  $j = \pm 1$  whereas total density has a square-lattice type pattern. The square-lattice soliton is quite similar to same of Figs. 8(a)-(d) and 9(e)-(h). However, the superstripe soliton of Figs. 10(e)-(h) has now acquired a square-lattice pattern in total density quite similar to a superstripe soliton of an SO-coupled spin-1 spinor BEC for  $\gamma = 8$  [23] in both ferromagnetic and polar phases. The stripe soliton



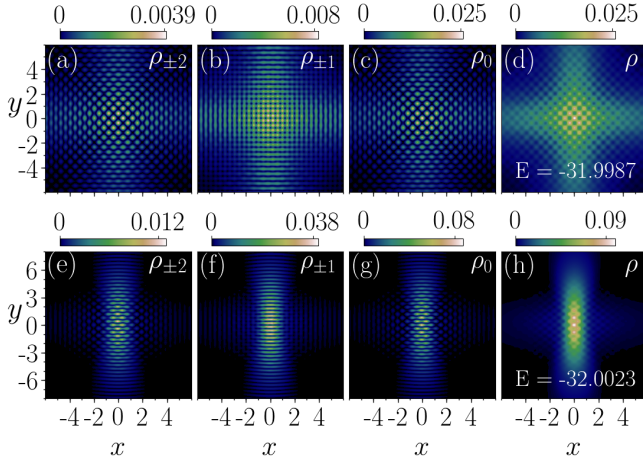


FIG. 10: (Color online) Contour plot of density of a square-lattice soliton of components (a)  $j = \pm 2$ , (b)  $j = \pm 1$ , (c)  $j = 0$ , and (d) total density with  $c_0 = -0.5$ ,  $c_1 = 0.025$ ,  $c_2 = -0.25$ , (polar phase)  $\gamma = 4$ ,  $E = -31.9987$ ; the same of a superstripe soliton for the same parameters in (e)-(h) with  $E = -32.0023$ .

with energy  $-32.0044$  and multi-ring soliton with energy  $-32.0009$  are not shown here.

#### D. Dynamical Stability

We confirm the dynamical stability of the stationary states of the SO-coupled spin-2 BEC discussed in Sec. III A-III C via a real-time propagation over an extended period of time up to  $t = 500$ . In addition to this, we have also tested the stability of these solutions by adding an initial random noise  $\delta\phi_j^{\text{noise}}$  to the respective order parameters at  $t = 0$  and then studying their real-time dynamics. We consider the random noise as

$$\delta\phi_j^{\text{noise}}(x, y) = 10^{-3} \sqrt{\mathcal{N}_j} R_g(x, y) e^{iR_u(x, y)}, \quad (15)$$

where  $\mathcal{N}_j = \int \rho_j(x, y) dx$ . The amplitude of this noise is randomized by random numbers  $R_g(x, y)$  which follow the Gaussian distribution, whereas phase of the noise is randomized by  $R_u(x, y)$  which follows a uniform probability distribution over the interval  $[0, 2\pi]$ . As an illustration, we consider the triangular-lattice soliton of Figs. 7(a)-(d) and the square-lattice soliton of Figs. 8(a)-(d). At  $t = 0$ ,  $\delta\phi_j^{\text{noise}}$  is added to the respective order parameters and the resultant order parameters are considered initial solutions to Eqs. (4a)-(4c), which are now solved (evolved) in real-time up to  $t = 100$ . The resultant component and total densities at  $t = 100$  are displayed in Figs. 11(a)-(d) and 11(e)-(h), respectively. The periodic density patterns survive with slightly different peak densities compared to the  $t = 0$  solutions, demonstrating the dynamical stability of the solitons.

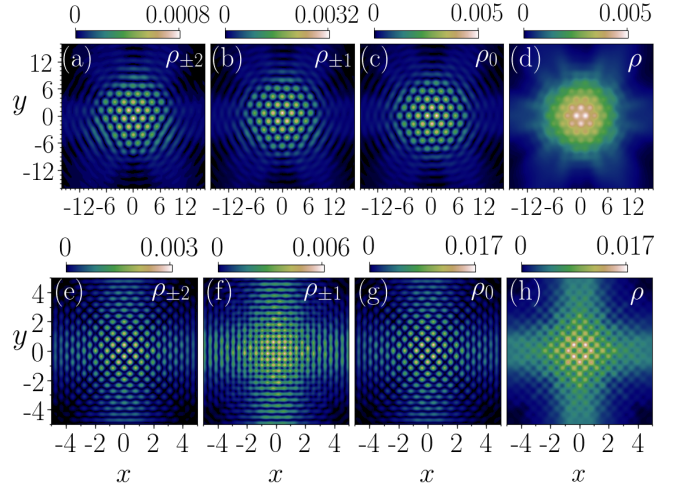


FIG. 11: (Color online) Contour plot of component densities of the triangular-lattice soliton of Figs. 7(a)-(d) for components (a)  $j = \pm 2$ , (b)  $j = \pm 1$ , (c)  $j = 0$ , and (d) total density after 100 units of time; the same of the square-lattice soliton of Figs. 8(a)-(d) for components (e)  $j = \pm 2$ , (f)  $j = \pm 1$ , (g)  $j = 0$ , and (h) total density, after real-time simulation over 100 units of time. The initial state used in real-time propagation is obtained by adding a random noise (15) to the stationary-state imaginary-time solutions shown in Figs. 7(a)-(d) for (a)-(d) and Figs. 8(a)-(d) for (e)-(h).

#### E. Bifurcations

In the non-interacting system, various solutions are completely degenerate, whereas on the introduction of interactions, solutions of Eqs. (4a)-(4c) exhibit a bifurcating behaviour. As the energies of these solutions are very close, to make the nature of these bifurcations clear, we calculate the difference  $\Delta E$  between total energy of the solution and the single-particle solution's energy, i.e.,  $-2\gamma^2$  as discussed in Sec. II C. A cut is now considered in the phase-diagram 4(a) at an appropriate  $c_2$ , say  $c_2 = 0.15$ , for the ferromagnetic phase, and  $\Delta E$  as a function of SO coupling strength  $\gamma$  is evaluated for the various solutions. Similarly, a cut at  $c_2 = 0.15$  for the cyclic phase in 4(b) and at  $c_2 = -0.15$  for the polar phase in 4(b) are considered. The resultant bifurcation plots showing  $\Delta E$  as a function of the SO-coupling strength  $\gamma$  are shown in Figs. 12(a)-(c) for the three magnetic phases. Bifurcation points agree with the critical points in the phase diagrams shown in Figs. 4(a)-(b).

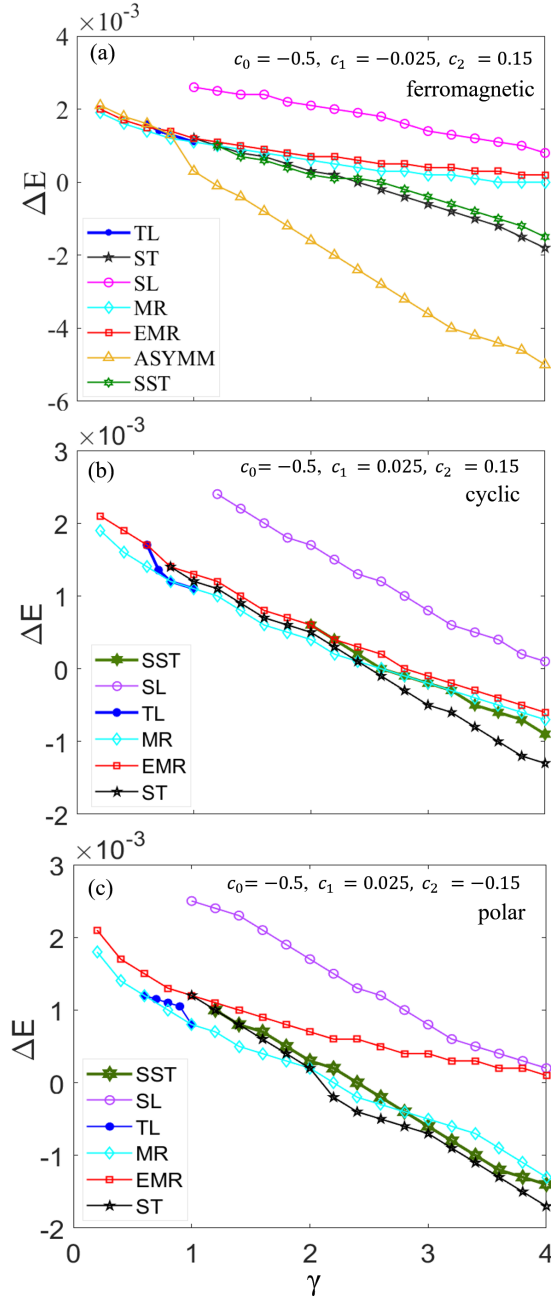


FIG. 12: (Color online) (a) The bifurcation diagram in the  $\Delta E$ - $\gamma$  plane for the ferromagnetic phase corresponding to a cut in the phase-diagram 4(a) at  $c_2 = 0.15$ . The same for the cyclic phase is shown in (b) by taking a cut at  $c_2 = 0.15$  in the phase-diagram 4(b). In the polar domain of phase diagram 4(b), a cut is taken at  $c_2 = -0.15$ , and bifurcation picture is shown in (c). The  $\Delta E = E + 2\gamma^2$ , where  $E$  is the energy of the state and  $-2\gamma^2$  is the single particle solution's energy, corresponding to various quasi-degenerate states are plotted by using different symbols as well as different colours. SST corresponds to the super-stripe similar to the state shown in 10(e)-(h), SL corresponds to the square-lattice similar to the state shown in 8(a)-(d), TL corresponds to the triangular-lattice similar to the state shown in 7(a)-(d), MR corresponds to the  $(-2, -1, 0, +1, +2)$ -type multi-ring solution similar to the state shown in 5(a)-(d), EMR corresponds to the  $(-1, 0, +1, +2, +3)$ -type excited-state multi-ring solution, ST corresponds to the stripe solution similar to the state shown in 9(a)-(d), ASYMM corresponds to the circularly-asymmetric solution similar to the state shown in 6(f)-(j).

## F. Moving $(-2, -1, 0, +1, +2)$ -type soliton

The SO coupling breaks the Galilean invariance of the mean-field model of the spinor BECs [35]. Explicitly, considering the Galilean transformation  $x' = x, y' = y - vt, t' = t$ , where  $v$  is the relative velocity along  $y$ -axis of primed coordinate system with respect to unprimed coordinate system, along with the following transformation of the wave function  $\psi' \rightarrow \phi$

$$\phi_j(x, y, t) = \psi'_j(x', y', t')e^{iv y' + i v^2 t'/2}, \quad (16)$$

we get from Eqs. (4a)-(4c)

$$i\partial_{t'}\psi'_{\pm 2} = \mathcal{H}\psi'_{\pm 2} + c_0\rho\psi'_{\pm 2} + c_1(F'_{\mp}\psi'_{\pm 1} \pm 2F'_z\psi'_{\pm 2}) + \frac{c_2}{\sqrt{5}}\Theta\psi'_{\mp 2} - i\gamma\partial_{\mp}\psi'_{\pm 1} + \gamma\psi'_{\pm 1}v, \quad (17a)$$

$$i\partial_{t'}\psi'_{\pm 1} = \mathcal{H}\psi'_{\pm 1} + c_0\rho\psi'_{\pm 1} + c_1\left(\sqrt{\frac{3}{2}}F'_{\mp}\psi'_0 + F'_{\pm}\psi'_{\pm 2} \pm F'_z\psi'_{\pm 1}\right) - \frac{c_2}{\sqrt{5}}\Theta\psi'_{\mp 1} - i\gamma\sqrt{\frac{3}{2}}\partial_{\mp}\psi'_0 - i\gamma\partial_{\pm}\psi'_{\pm 2} + \gamma\left(\sqrt{\frac{3}{2}}\psi'_0 + \psi'_{\pm 2}\right)v, \quad (17b)$$

$$i\partial_{t'}\psi'_0 = \mathcal{H}\psi'_0 + c_0\rho\psi'_0 + c_1\sqrt{\frac{3}{2}}(F_{-}\psi'_{-1} + F_{+}\psi'_{+1}) + \frac{c_2}{\sqrt{5}}\Theta\psi'_0 - i\gamma\sqrt{\frac{3}{2}}\gamma\partial_{+}(\psi'_{+1} + \psi'_{-1}) + \gamma\sqrt{\frac{3}{2}}(\psi'_{+1} + \psi'_{-1})v, \quad (17c)$$

where  $\partial_{\pm} = (\partial_{x'} \pm i\partial_{y'})$ . These equations are distinct from Eqs. (4a)-(4c) indicating a breakdown of the Galilean invariance. For an SO-coupled spin-2 BEC, the moving solitons are the stationary solutions of Eqs. (17a)-(17c) multiplied by a factor of  $e^{ivy}$ . The structure of the moving soliton depends on the magnitude as well as direction of velocity. Here we study the fate of a moving  $(-2, -1, 0, +1, +2)$ -type multi-ring soliton by solving Eqs. (17a)-(17c) numerically, for small SO-coupling strength, as the velocity is increased. For example, considering  $c_0 = -2.5, c_1 = -0.025, c_2 = 0.25, \gamma = 0.5$  with (a)  $v = 0.03$  and (b)  $v = 0.1$ , the component densities of the moving solitons are shown in Figs. 13(a)-(e) and (f)-(j), respectively. The structure of the moving soliton at two different velocities are quite distinct as can be seen in Fig. 13. With the increase of velocity along  $y$  axis, component phase-singularities move along  $x$  axis to region of low density away from the center, resulting in component densities without any vortex core at velocity  $v = 0.1$ . For  $c_0 = -2.5, c_1 = -0.025, c_2 = 0.25, \gamma = 0.5$ , a self-trapped moving soliton with  $v > 0.3$  does not exist.

We have also studied the head-on collision of these solitons. At low velocities, the collision is inelastic while the solitons come close to each other interact and form a bound entity and never come out. On the other hand, at large initial velocities the collision is quasi elastic; in this case the solitons tend to pass through each other without any change of velocity. For example, the head-on collision between the solitons moving with  $|v| = 0.03$  and  $c_0 = -2.5, c_1 = -0.025, c_2 = 0.25, \gamma = 0.5$ , is shown

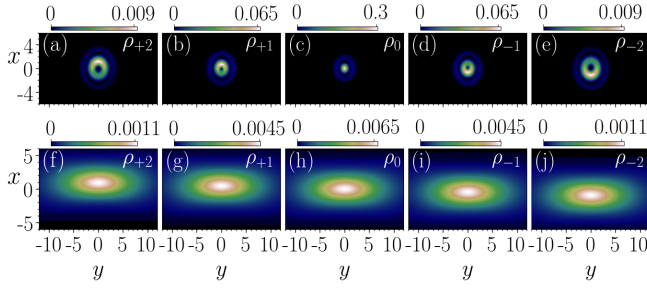


FIG. 13: (Color online) Contour plot of density of components (a)  $j = +2$ , (b)  $j = +1$ , (c)  $j = 0$ , (d)  $j = -1$ , and (e)  $j = -2$  with  $c_0 = -2.5$ ,  $c_1 = -0.025$ ,  $c_2 = 0.25$ , and  $\gamma = 0.5$  moving with  $v = 0.03$  along  $+y$ ; the same densities for velocity  $v = 0.1$  in (f)-(j).

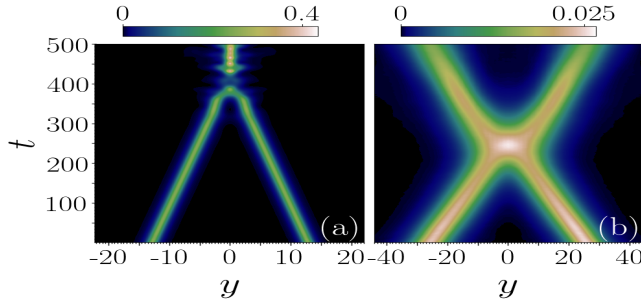


FIG. 14: (Color online) Contour plot of total density  $\rho(0, y, t)$  as a function of  $y$  and  $t$  during the head-on collision between the two solitons with  $c_0 = -2.5$ ,  $c_1 = -0.025$ ,  $c_2 = 0.25$ ,  $\gamma = 0.5$  moving with velocity (a)  $|v| = \pm 0.03$  and (b)  $|v| = \pm 0.1$  along  $y$  axis in opposite direction.

in Fig. 14(a) through a contour plot of time evolution of total density  $\rho(0, y, t)$  in the  $t - y$  plane. Similarly, a quasi-elastic collision between two solitons moving with velocity  $|v| = 0.1$  is shown in Fig. 14(b). The collision dynamics is consistent with the similar observations for two SO-coupled spin-1 BECs [17].

#### IV. SUMMARY AND CONCLUSION

We have demonstrated the emergence of various self-trapped stable solitons with supersolid-like crystallization in a quasi-2D SO-coupled spin-2 BEC employing analytic consideration and numerical solution of the un-

derlying mean-field GP equation. The minimization of interaction and SO-coupling energies leads to the permissible winding-number combinations for axisymmetric solitons. In the absence of interactions, we consider the eigenfunctions of the single-particle Hamiltonian to construct the order parameters consistent with multi-ring, stripe, triangular-, and square-lattice density profiles. In the presence of (attractive) interactions, we find that various types of solitons with spatially-periodic modulation in density appears, including the ones inferred from a study of the eigenfunctions of the single-particle Hamiltonian, due to an interplay of SO-coupling and interactions.

The ground state for a small SO-coupling strength ( $\gamma \approx 0.5$ ) is a radially symmetric multi-ring soliton for weakly-ferromagnetic, cyclic and polar interactions, whereas for a sufficiently strong-ferromagnetic interaction, circularly-asymmetric soliton emerges as the ground state. For intermediate SO-coupling strengths ( $\gamma \approx 1$ ), in addition to the axisymmetric soliton, there could exist a triangular-lattice soliton with a hexagonal crystallization of matter in the soliton, explicit in both component and total densities. On increasing the SO-coupling further, one could have five quasi-degenerate solitons, e.g. a multi-ring soliton, a square-lattice soliton, a stripe soliton and a superstripe soliton, in all the magnetic phases, and also circularly-asymmetric soliton in the ferromagnetic phase. The quasi-degeneracy between the states is in general lifted with either a decrease in the SO-coupling strength  $\gamma$  or an increase in the attractive spin-independent interaction strength  $|c_0|$ . We also introduced the Galilean-transformed model to study the moving solitons and the head-on collision dynamics between two such solitons. A head-on collision between the two solitons is inelastic at low velocities and the two solitons can form a bound entity. At large velocities the collision is quasi elastic, and the solitons pass through each other without a substantial change of velocity.

#### Acknowledgments

SG acknowledges the support of the Science & Engineering Research Board (SERB), Department of Science and Technology, Government of India under the Project ECR/2017/001436. SKA acknowledges partial support by the CNPq (Brazil) grant 301324/2019-0, and by the ICTP-SAIFR-FAPESP (Brazil) grant 2016/01343-7.

#### Appendix

For a spin-2 BEC, the spin-dependent interaction energy is given as [1]

$$E_{\text{int}} = \int \left( \frac{c_1}{2} |\mathbf{F}|^2 + \frac{c_2}{2} |\Theta|^2 \right) r dr d\theta \quad (18)$$

Using *ansatz* (7), the contribution of phase dependent terms in the spin dependent interaction energy (18) can be

written as

$$\begin{aligned}
E_{\text{int}}^{\text{phase}} = & 2\sqrt{6}c_1 \int R_0 R_{+1}^2 R_{+2} r dr \int \cos[(w_0 - 2w_{+1} + w_{+2})\theta + (\alpha_0 - 2\alpha_{+1} + \alpha_{+2})] d\theta + 2\left(3c_1 - \frac{c_2}{5}\right) \int R_0^2 R_{+1} R_{-1} r dr \\
& \times \int \cos[(w_{+1} + w_{-1} - 2w_0)\theta + (\alpha_{+1} + \alpha_{-1} - 2\alpha_0)] d\theta + 2\sqrt{6}c_1 \int R_0 R_{-1}^2 R_{-2} r dr \int \cos[(w_0 + w_{-2} - 2w_{-1})\theta \\
& + (\alpha_0 + \alpha_{-2} - 2\alpha_{-1})] d\theta \\
& + 2\sqrt{6}c_1 \int R_0 R_{+1} R_{+2} R_{-1} r dr \int \cos[(w_{+2} + w_{-1} - w_0 - w_{+1})\theta + (\alpha_{+2} + \alpha_{-1} - \alpha_0 - \alpha_{+1})] d\theta \\
& + 2c_1 \sqrt{6} \int R_0 R_{+1} R_{-1} R_{-2} r dr \int \cos[(w_{+1} + w_{-2} - w_0 - w_{-1})\theta + (\alpha_{+1} + \alpha_{-2} - \alpha_0 - \alpha_{-1})] d\theta \\
& + 4\left(c_1 - \frac{c_2}{5}\right) \int R_{+1} R_{+2} R_{-1} R_{-2} r dr \int \cos[(w_{+2} + w_{-2} - w_{+1} - w_{-1})\theta + (\alpha_{+2} + \alpha_{-2} - \alpha_1 - \alpha_{-1})] d\theta \\
& + \frac{2c_2}{5} \int R_{+2} R_{-2} R_0^2 r dr \int \cos[(2w_0 - w_{+2} - w_{-2})\theta + (2\alpha_0 - \alpha_{+2} - \alpha_{-2})] d\theta.
\end{aligned} \tag{19}$$

A typical  $\theta$ -dependent term in Eq. (19) can be written as [36]

$$\int_0^{2\pi} \cos(w_s \theta + \alpha_s) d\theta = \frac{\sin(2\pi w_s + \alpha_s)}{w_s} - \frac{\sin \alpha_s}{w_s}, \tag{20}$$

where  $w_s$  and  $\alpha_s$ , represent any of the linear combinations of  $w_j$ 's and  $\alpha_j$ 's appearing as arguments of cosine, respectively. As  $w_s$  can only be an integer including zero, the absolute value of integral (20) is  $2\pi$  if  $w_s = 0$  and  $\alpha_s$  is an integer multiple of  $\pi$ . The exact values of  $\alpha_s$  has to be determined by minimizing energy (19) with  $w_s = 0$ . The permitted independent winding number relations thus are

$$w_{+1} + w_{-1} - 2w_0 = 0, \quad w_{+2} + w_{-2} - w_{+1} - w_{-1} = 0, \quad w_0 + w_{-2} - 2w_{-1} = 0. \tag{21}$$

The energy contribution from SO-coupling terms, obtained by using ansatz (7), is

$$\begin{aligned}
E_{\text{so}} = & \int dx dy \sum_j \phi_j^* \Gamma_j \\
= & \gamma \int d\mathbf{r} \left[ R_{+2} e^{i[(w_{+1} - w_{+2} - 1)\theta + (\alpha_{+1} - \alpha_{+2})]} \left[ \frac{\partial R_{+1}}{\partial r} + w_{+1} \frac{R_{+1}}{r} \right] + R_{-1} e^{i[(w_{-2} - w_{+1} - 1)\theta + (\alpha_{-2} - \alpha_{-1})]} \left[ \frac{\partial R_{-2}}{\partial r} + \frac{w_{-2} R_{-2}}{r} \right] \right. \\
& + R_{+1} e^{i[(w_{+2} - w_{+1} + 1)\theta + (\alpha_{+2} - \alpha_{+1})]} \left[ \frac{-\partial R_{+2}}{\partial r} + \frac{w_{+2} R_{+2}}{r} \right] + R_{-2} e^{i[(w_{-1} - w_{-2} + 1)\theta + (\alpha_{-1} - \alpha_{-2})]} \left[ \frac{-\partial R_{-1}}{\partial r} + w_{-1} \frac{R_{-1}}{r} \right] \Big] \\
& + \sqrt{\frac{3}{2}} \gamma \int d\mathbf{r} \left[ R_{+1} e^{i[(w_0 - w_{+1} - 1)\theta + (\alpha_0 - \alpha_{+1})]} \left[ \frac{\partial R_0}{\partial r} + \frac{w_0 R_0}{r} \right] + R_{-1} e^{i[(w_0 - w_{-1} + 1)\theta + (\alpha_0 - \alpha_{-1})]} \left[ \frac{-\partial R_0}{\partial r} + \frac{w_0 R_0}{r} \right] \right. \\
& + R_0 e^{i[(w_{-1} - w_0 - 1)\theta + (\alpha_{-1} - \alpha_0)]} \left[ \frac{\partial R_{-1}}{\partial r} + \frac{w_{-1} R_{-1}}{r} \right] + R_0 e^{i[(w_{+1} - w_0 + 1)\theta + (\alpha_{+1} - \alpha_0)]} \left[ \frac{-\partial R_{+1}}{\partial r} + \frac{w_{+1} R_{+1}}{r} \right] \Big],
\end{aligned} \tag{22}$$

where  $\mathbf{r} \equiv \{x, y\} \equiv \{r, \theta\}$ . Again, a minimization of  $E_{\text{so}}$  requires that

$$w_{+2} - w_{+1} + 1 = 0, \quad w_{+1} - w_0 + 1 = 0, \tag{23}$$

$$w_{-2} - w_{-1} - 1 = 0, \quad w_{-1} - w_0 - 1 = 0, \tag{24}$$

and linear combinations of  $\alpha_j$ 's appearing in Eq. (22) are integer multiple of  $\pi$ . The winding number relations in Eq. (21) are not independent as all can be obtained from winding number relations in Eqs. (23) and (24).

- 
- [1] Y. Kawaguchi and M. Ueda, Phys. Rep. **520**, 253 (2012); D. M. Stamper-Kurn and M. Ueda Rev. Mod. Phys. **85**, 1191 (2013).  
[2] Y.-J. Lin, K. Jiménez-García, and I.B. Spielman, Nature (London) **471**, 83 (2011).  
[3] J.-Y. Zhang, S.-C. Ji, Z. Chen, L. Zhang, Z.-D. Du, B. Yan, G.-S. Pan, B. Zhao, Y.-J. Deng, H. Zhai, S. Chen, and J.-W. Pan, Phys. Rev. Lett. **109**, 115301 (2012); C. Qu, C. Hamner, M. Gong, C. Zhang, and P. Engels, Phys. Rev. A **88**, 021604(R) (2013); A. J. Olson, S.-J.

- Wang, R. J. Niffenegger, C.-H. Li, C. H. Greene, and Y. P. Chen, Phys. Rev A **90**, 013616 (2014).  
[4] Z. Wu, L. Zhang, W. Sun, X.-T. Xu, B.-Z. Wang, S.-C. Ji, Y. Deng, S. Chen, X.-J. Liu, and J.-W. Pan, Science, **354**, 83 (2016).  
[5] D.L. Campbell, R.M. Price, A. Putra, A. Valdés-Curiel, D. Trypogeorgos, and I.B. Spielman, Nature Commun. **7**, 10897 (2016); X. Luo, L. Wu, J. Chen, Q. Guan, K. Gao, Zhi-Fang Xu, L. You, and R. Wang, Scientific Rep. **6**, 18983 (2016).



- [6] M. C. Beeler, R. A. Williams, K. Jiménez-García, L. J. LeBlanc, A. R. Perry, and I. B. Spielman, *Nature (London)* **498**, 201 (2013).
- [7] M. Levin and A. Stern, *Phys. Rev. Lett.* **103**, 196803 (2009).
- [8] C.-H. Li, C. Qu, R. J. Niffenegger, S.-J. Wang, M. He, D. B. Blasing, A. J. Olson, C. H. Greene, Y. Lyanda-Geller, Q. Zhou, C. Zhang, and Y. P. Chen, *Nature Commun.* **10**, 375 (2019).
- [9] V. Galitski and I.B. Spielman, *Nature (London)* **494**, 49 (2013).
- [10] E. I. Rashba, *Fiz. Tverd. Tela* **2**, 1224 (1960); [English Transla.: *Sov. Phys. Solid State* **2**, 1109 (1960).]
- [11] G. Dresselhaus, *Phys. Rev.* **100**, 580 (1955).
- [12] Y. Li, L. P. Pitaevskii, and S. Stringari, *Phys. Rev. Lett.* **108**, 225301 (2012).
- [13] B. M. Anderson, I. B. Spielman, and G. Juzeliunas, *Phys. Rev. Lett.* **111**, 125301 (2013); Z.-F. Xu, L. You, and M. Ueda, *Phys. Rev. A* **87**, 063634 (2013).
- [14] R. Y. Chiao, E. Garmire, and C. H. Townes, *Phys. Rev. Lett.* **13**, 479 (1964).
- [15] Y. S. Kivshar and B. A. Malomed, *Rev. Mod. Phys.* **61**, 763 (1989).
- [16] Y. V. Kartashov, G. E. Astrakharchik, B. A. Malomed, and L. Torner, *Nature Rev. Phys.* **1**, 185 (2019).
- [17] S. Gautam and S.K. Adhikari, *Phys. Rev. A* **95**, 013608 (2017).
- [18] S. Gautam, and S.K. Adhikari, *Phys. Rev. A* **97**, 013629 (2018).
- [19] Y. Xu, Y. Zhang, and B. Wu, *Phys. Rev. A* **87**, 013614 (2013); L. Salasnich and B. A. Malomed, *Phys. Rev. A* **87**, 063625 (2013).
- [20] L. Salasnich, W. B. Cardoso, and B. A. Malomed, *Phys. Rev. A* **90**, 033629 (2014); H. Sakaguchi, B. Li, and B. A. Malomed, *Phys. Rev. E* **89**, 032920 (2014); H. Sakaguchi and B. A. Malomed, *Phys. Rev. E* **90**, 062922 (2014).
- [21] Y.-C. Zhang, Z.-W. Zhou, B.A. Malomed, and H. Pu, *Phys. Rev. Lett.* **115**, 253902 (2015).
- [22] S. Gautam. and S.K. Adhikari, *Laser Phys. Lett.* **12**, 045501 (2015).
- [23] S.K. Adhikari, *Phys Rev A* **103**, L011301 (2021) ; S.K. Adhikari, *Phys Lett A* **388**, 127042 (2021).
- [24] Z. F. Xu, Y. Kawaguchi, L. You, and M. Ueda, *Phys. Rev. A* **86**, 033628 (2012).
- [25] Z. F. Xu, R. Lü, and L. You, *Phys. Rev. A* **83**, 053602 (2011).
- [26] M. Schmitt, M. Wenzel, F. Böttcher, I. Ferrier-Barbut, and T. Pfau, *Nature (London)* **539**, 259 (2016); F. Böttcher, J.-N. Schmidt, M. Wenzel, J. Hertkorn, M. Guo, T. Langen, and T. Pfau, *Phys. Rev. X* **9**, 011051 (2019); L. Chomaz, D. Petter, P. Ilzhöfer, G. Natale, A. Trautmann, C. Politi, G. Durastante, R. M. W. van Bijnen, A. Patscheider, M. Sohmen, M. J. Mark, and F. Ferlaino, *Phys. Rev. X* **9**, 021012 (2019); L. Tanzi, E. Lucioni, F. Famà, J. Catani, A. Fioretti, C. Gabbanini, R. N. Bisset, L. Santos, and G. Modugno, *Phys. Rev. Lett.* **122**, 130405 (2019).
- [27] G. Natale, R. M. W. van Bijnen, A. Patscheider, D. Petter, M. J. Mark, L. Chomaz, F. and Ferlaino, *Phys. Rev. Lett.* **123**, 050402 (2019); L. Tanzil, S. M. Roccuzzo, E. Lucioni, F. Famà, A. Fioretti, C. Gabbanini, G. Modugno, A. Recati, and S. Stringari, *Nature (London)* **574**, 382 (2019); M. Guo, Fabian Böttcher, J. Hertkorn, J.-N. Schmidt, M. Wenzel, H. P. Büchler, T. Langen, and T. Pfau, *Nature (London)* **574**, 386 (2019); J. Hertkorn, F. Böttcher, M. Guo, J. N. Schmidt, T. Langen, H. P. Büchler, and T. Pfau, *Phys. Rev. Lett.* **123**, 193002 (2019).
- [28] J.-R. Li, J. Lee, W. Huang, S. Burchesky, B. Shteynas, F. Ç. Top, A. O. Jamison, and W. Ketterle, *Nature (London)* **543**, 91 (2017).
- [29] A. Putra, F. Salces-Cárcoba, Y. Yue, S. Sugawa, and I. B. Spielman, *Phys. Rev. Lett.* **124**, 053605 (2020).
- [30] Y. Li, G. I. Martone, L. P. Pitaevskii, and S. Stringari, *Phys. Rev. Lett.* **110**, 235302 (2013).
- [31] C.V. Ciobanu, S.-K. Yip, and T.-L. Ho *Phys. Rev. A* **61**, 033607 (2000).
- [32] M. Ueda and M. Koashi, *Phys. Rev. A* **65**, 063602 (2002).
- [33] H. Zhai, *Int. J. Mod. Phys. B* **26**, 1230001 (2012); H. Zhai, *Rep. Prog. Phys.* **78**, 026001 (2015).
- [34] P. Banger, P. Kaur, A. Roy, and S. Gautam, *arXiv:2011.08892*.
- [35] S. Gautam and S. K. Adhikari *Phys. Rev. A* **91**, 063617 (2015).
- [36] W. Han, X. Zhang, S. Song, H. Saito, W. Zhang, W. Liu, and S. Zhang, *Phys. Rev. A* **94**, 033629 (2016).